Magnetic and photocatalytic properties of BiFeO$_3$ nanoparticles formed during the heat treatment of hydroxides coprecipitated in a microreactor with intense swirling flows

Olga V. Proskurina[1,2,a], Ksenia I. Babich[1,2,b], Sofia M. Tikhanova[1,2,c], Kirill D. Martinson[1,2,d], Vladimir N. Nevedomskiy[1,e], Valentin G. Semenov[3,f], Rufat Sh. Abiev[1,2,g], Victor V. Gusarov[1,h]

[1]Ioffe Institute, St. Petersburg, Russia
[2]St. Petersburg State Institute of Technology, St. Petersburg, Russia
[3]St. Petersburg State University, St. Petersburg, Russia

[a]proskurinaov@mail.ru, [b]babich3111@gmail.com, [c]tihanova.sof@gmail.com, [d]martinsonkirill@mail.ru,
[e]nevedom@mail.ioffe.ru, [f]val_sem@mail.ru, [g]abiev.rufat@gmail.com, [h]victor.v.gusarov@gmail.com

Corresponding author: O. V. Proskurina, proskurinaov@mail.ru

ABSTRACT In this work, hydroxide deposition in a microreactor with intensively swirling flows was used to obtain BiFeO$_3$, followed by heat treatment of co-precipitated bismuth and iron hydroxides. The study of the formation of nanocrystalline bismuth orthoferrite was carried out using a set of methods: EDXMA, TEM, XRD, ^{57}Fe Mössbauer spectroscopy, DRS, etc. The photocatalytic activity and magnetic characteristics of the material were determined. It is shown that during heat treatment of hydroxide precipitation for 1 minute at a temperature of 530 °C, BiFeO$_3$ nanocrystals with an average crystallite size of 14±7 nm are formed. It was found that the resulting BiFeO$_3$ nanopowder is represented by agglomerates of individual nanoparticles. The saturation magnetization and residual magnetization values of these bismuth orthoferrite nanoparticles are 2.31 and 0.48 emu/g, respectively. According to the DRS results, band gap energy for the samples calculated at 530, 515, and 500 °C were 1.82, 1.86, and 1.91 eV, respectively, which ensures strong absorption of visible light by the samples. The sample showed higher photocatalytic activity in the X-ray amorphous state compared with nanocrystalline BiFeO$_3$ in the process of Fenton-like discoloration of methyl violet under the action of visible light with reaction rate constants of the pseudo-first order 0.0256 and 0.0072 min^{-1}, respectively.

KEYWORDS microreactor with intensively swirling flows, nanocrystals, nanoparticles, bismuth ferrite, photocatalysis, Fenton-like reactions.

1. Introduction

Bismuth orthoferrite BiFeO$_3$ is a well-known multiferroic and continues to attract the attention of researchers due to the promising functional properties of the materials obtained from it [1–3]. Magnetic [4–6], electrophysical [7, 8], optical [9,10], photocatalytic properties [11–14], photovoltaic [15], and the use of bismuth orthoferrite as a sensor material are actively investigated [16–19].

The morphology, sizes and structure of bismuth orthoferrite nanoparticles, the presence and amount of impurity phases can significantly affect the functional properties of the materials obtained from them [20–23].

Methods for the synthesis of bismuth orthoferrite nanopowders are constantly being developed in order to provide the characteristics required to obtain materials with certain functional properties. Bismuth orthoferrite is obtained by various methods, in particular, the solution combustion method [24–26], hydrothermal synthesis [27–29], hydrothermal microwave [30], solid-phase synthesis [31–33], the method of mechanical activation [34] is used Nevertheless, the problem of obtaining phase-pure nanocrystalline bismuth orthoferrite powders remains relevant [35–37].

A promising direction for the production of oxide nanoparticles is the use of microreactor technology [38]. Free impinging-jets microreactor have been successfully used to obtain nanocrystals of complex oxides [39, 40]. In such microreactors, self-organizing spatially separated reaction zones with dimensions of about hundreds of nanometers are formed, in which nanoparticles with certain size parameters are formed [41, 42]. When producing nanocrystalline bismuth orthoferrite using a free impinging-jets microreactor, no impurity phases are detected [43].

Swirling-flow microreactors have found wide application for the production of various oxide nanoparticles. In such microreactors, a high level of specific energy dissipation rate is created (on the order of 2–35 kW/kg), which, in turn, contributes to the intensification of the micro-mixing process [44, 45].

In [46, 47], various types of microreactors were used to obtain nanocrystalline bismuth orthoferrite, but studies of the functional properties of bismuth orthoferrite were not carried out The purpose of this work was to determine the magnetic and photocatalytic properties of nanocrystalline bismuth orthoferrite obtained by heat treatment of bismuth and iron hydroxides co-deposited in a microreactor with intensively swirling flows.

2.   Experimental

To obtain bismuth orthoferrite, bismuth and iron nitrates $Bi(NO_3)_3 \cdot 5H_2O$ and $Fe(NO_3)_3 \cdot 9H_2O$ of analytical purity were used. Bismuth nitrate was dissolved in 7 mL of 4 M HNO_3 with stirring for 10 minutes and heating to 70 °C. Then, a portion of iron nitrate was added to the resulting solution with stirring. Weights of salts were calculated to prepare 3 g of bismuth ferrite. After stirring for 10 minutes, 130 mL of distilled water was added and stirred for another 20 minutes. Separately, 1 L of 4 M NaOH solution was prepared. The resulting solutions were used for co-precipitation of bismuth and iron(III) hydroxides in an one-step microreactor with intensively swirling flows (MRISF-1). Co-precipitation was carried out at a temperature of about 22 °C and atmospheric pressure.

A solution of bismuth and iron nitrates was fed into MRISF-1 into one of the tangential inlet pipes, and a solution of NaOH antisolvent into an axial inlet pipe; both solutions were supplied with the same flow rates of 2.1 L/min (Fig. 1).

As a result of solutions intensive mixing in the microreactor, a suspension of co-precipitated bismuth and iron hydroxides was obtained, which was then washed with distilled water using centrifugation and intermediate dispersion using an ultrasonic bath in order to better wash the sediments from alkali residues. The washed samples were dried at 70 °C for 24 hours.

The dried samples were heated in a tubular furnace in a platinum crucible in the "annealing-quenching" mode for 1 minute at temperatures of 500, 515 and 530 °C. The samples were designated "HT 500 °C", "HT 515 °C" and "HT 530 °C".
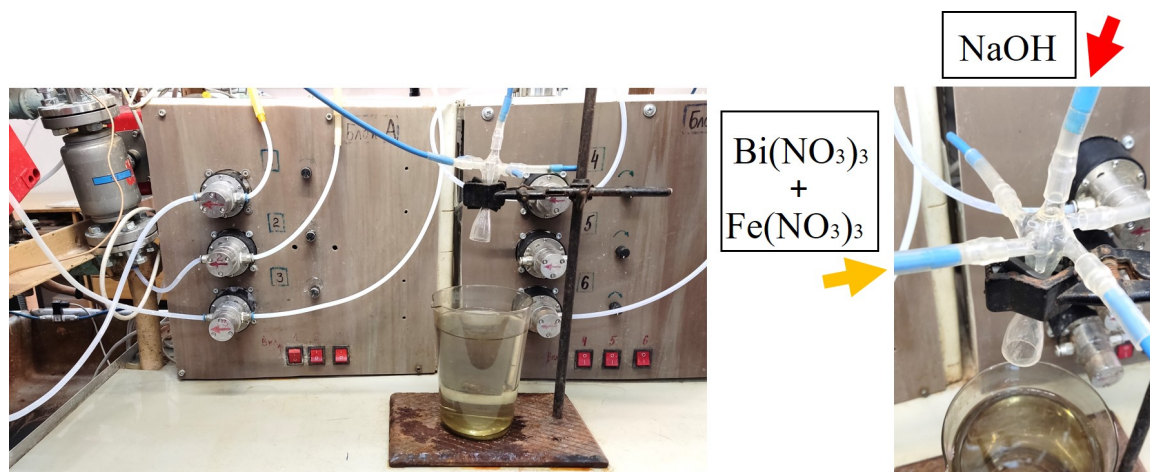
FIG. 1. One-step microreactor with intensively swirling flows:(a) experimental rig; (b) schematic of solutions supply into inlet pipes of the MRISF-1

3.   Characterization

Powders were characterized by several methods. X-ray diffraction patterns were taken on a Rigaku SmartLab 3 (Rigaku Corporation, Japan) powder diffractometer (CuK_α radiation) in the angle range $2\theta = 20 - 60°$ with a step of $0.01°$ and a speed of 0.1 °/min. The average crystallite size was determined using the SmartLab Studio II software package from Rigaku. The size distribution of crystallites was determined by the method of fundamental parameters in the approximation of a lognormal distribution model using the SmartLab Studio II software package for reflection 024.

The elemental composition of the samples was determined using a Tescan Vega 3 SBH scanning electron microscope (Tescan, Czech Republic) with an energy dispersive X-ray spectroscopy (EDX) Oxford Instruments INCA x-act X-ray microanalysis attachment (Oxford Instruments, Oxford, UK).

Transmission electron microscopy (TEM) studies with the determination of microdiffraction of the samples were performed using a JEOL JEM-2100F microscope (JEOL Ltd., Akishima, Tokyo, Japan) at an accelerating voltage of 200 kV. Samples for research were prepared by preliminary dispersion of the initial powder in ethyl alcohol in an ultrasonic bath for 15 minutes, followed by deposition on a supporting film.

To study the magnetic properties and magnetic structure, Mössbauer spectroscopy was used, which is an informative method for studying the properties of iron-containing materials and differences in the local environments of iron atoms. The measurements were carried out on a Mössbauer spectrometer from WISSEL on the ^{57}Fe isotope with registration in the geometry of transmission of γ-radiation through the sample under study from a ^{57}Co source in a rhodium (Rh) matrix. The reference signal in the motion system of the Doppler modulator in the spectrometer had the shape of a triangle to set the speed with constant acceleration. The speed scale was calibrated using α-iron foil at room temperature. The Mössbauer spectra of the samples under study were measured at room temperature. Mathematical processing of the spectra was carried out using a program that describes spectral lines by Lorentzian-shaped peaks and minimization using the least squares method. In the procedure for minimizing the functional $\chi 2$, the program searches for optimal values of the parameters of spectral lines, namely, widths, intensities and positions. The parameters of hyperfine interactions were calculated from the positions of the lines: IS – isomer chemical shift, QS – quadrupole splitting, H$_{eff}$– effective magnetic field.

The magnetic characteristics of a bismuth ferrite sample were studied using a Lake Shore 7410 vibration magnetometer at room temperature (25 °C) in a field range of up to 30,000 Oe using a standard measuring cell.

The light absorption ability of the samples was investigated by diffuse reflectance spectra (DRS) in the UV-visible region were recorded at room temperature in the range of 400–800 nm using an AvaSphere-30-Refl integrating sphere.

The band gap energy (E$_g$) was calculated from the plot of the Kubelka–Munk function:

$$F(R) = \frac{(1 - R)^n}{2R} = \frac{K}{S},$$

where K is the molar absorption coefficient, S is the scattering factor, and R is the reflectance of the material. The value of n is determined by the nature of the sample ($n = 2$ for direct allowed transitions and $n = 1/2$ for indirect allowed transitions)

The photocatalytic activity of the samples was studied in the process of photocatalytic and photo-Fenton-like degradation of methyl violet (MV) under visible-light irrigation $\lambda_{\max} = 410$ nm (Fig. 2). In a typical manner described previously [48], the 1.5 mg of the catalyst was suspended in 1 mL of distilled water and added to MV solution (3 mmol/L). Before visible light irradiation, the 50 mL reaction solutions were magnetically stirred in the darkness for 30 min to ensure the adsorption-desorption equilibrium. After this stage 10 mL of H$_2$O$_2$ solution (20 mmol/L) was added to examine the photo-Fenton-like activity. At appropriate time intervals, 2 mL of the solution was collected to spectrophotometrically determine the concentration of the dye using AvaLight-XE light source and AvaSpec-ULS2048 spectrometer.
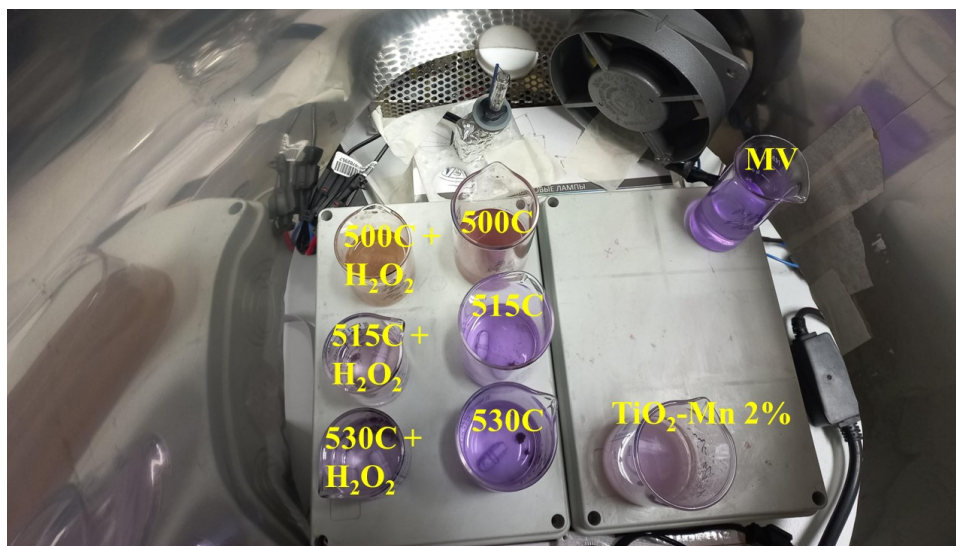
FIG. 2. Solutions of MV dye with a catalyst in the process of studying photocatalytic activity

4. Results and discussion

Energy-dispersive X-ray spectroscopy data of all samples showed that the atomic ratio of bismuth and iron in all samples after heat treatment remains at the same level (Bi : Fe = (52±2) : (48±2)), which, within the error, corresponds to the ratio specified during synthesis , corresponding to the stoichiometry of BiFeO$_3$.

X-ray diffractometry data of heat-treated samples are shown in Fig. 3. The diffraction pattern of a sample heat-treated at 500 °C has an X-ray amorphous appearance. The diffraction pattern of the sample heat-treated at 515 °C shows the appearance of reflections corresponding to bismuth orthoferrite (ICSD code 163688). The diffraction pattern of the sample heat-treated at 530 °C shows reflections of crystalline bismuth orthoferrite and no X-ray amorphous halo. For this sample, in the inset in Fig. 3, it is shown the crystallite size distribution determined from reflection 024. The weighted average value of the $BiFeO_3$ crystallite size for the sample heat-treated at 530 °C was 14 ± 7 nm.
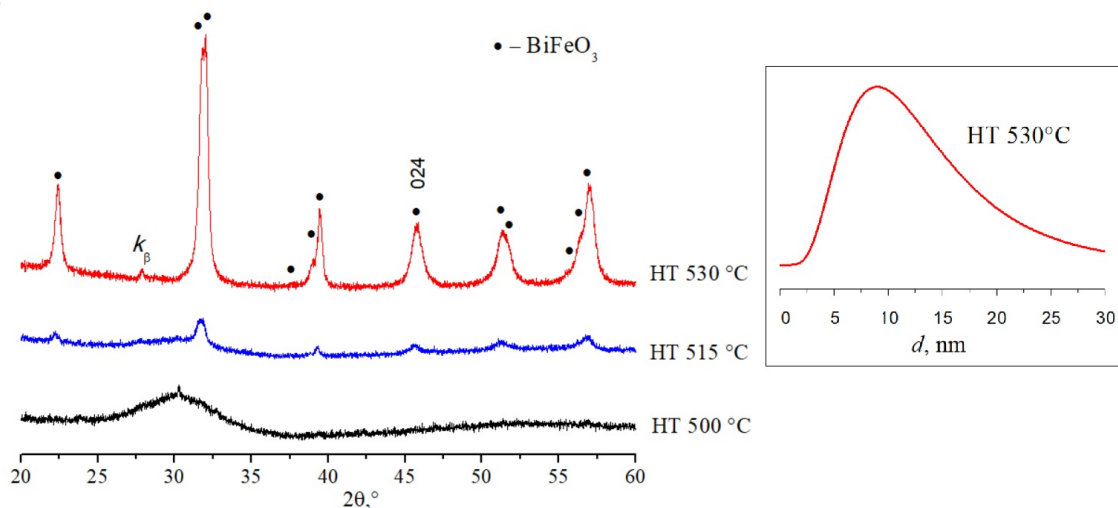
FIG. 3. X-ray diffraction patterns of samples after heat treatment and crystallite size distribution according to reflection 024 for a sample heat treated at 530 °C

TEM micrographs of bismuth orthoferrite samples heat-treated at three different temperatures are presented in Fig. 4.

Images of samples heat-treated at 500, 515 and 530 °C are presented in Figures 4a, 4b, 4c, respectively. All samples are nanoparticles assembled into aggregates. The electron diffraction image in Fig. 4a confirms that the sample is X-ray amorphous, since the electron diffraction (SAED) image in Fig. 4a, wide circles are visible from the carbon substrate and the X-ray amorphous sample. Electron microdiffraction data from samples "HT 515 °C" and "HT 530 °C" confirm the polycrystalline nature of the samples, as well as the presence of a certain amount of X-ray amorphous phase in the sample "HT 515 °C". For the "HT 530 °C" sample in Fig. 4c on the right it is also shown a dark-field image in which bright spots corresponding to $BiFeO_3$ nanocrystals of various sizes are visible.

Analysis of the results of studying the crystallization of $BiFeO_3$ by TEM (Fig. 4) allows us to conclude that the formation of bismuth ferrite nanocrystals occurs according to the following mechanism. After dehydration of a mixture of amorphous bismuth and iron hydroxides and the formation of crystalline $BiFeO_3$ nuclei (see Fig. 4a), their growth occurs due to the coherent addition of the clusters that make up the amorphous phase to crystalline particles of bismuth ferrite. Such crystal growth is stopped if growing $BiFeO_3$ crystals collide with each other without oriented intergrowth along the faces (Fig. 5).

Another reason for the suspension of crystal growth is the depletion of the amorphous substance within which it grows. With this mechanism of crystallite growth, their shape and size will be largely determined by both the intensity of the nucleation process and the geometric parameters of the amorphous phase particles. In this case, along with small $BiFeO_3$ nanocrystals of regular shape, relatively large crystals with complex morphology will be formed (Fig. 4c). It should be noted that a similar nature of the formation of $BiFeO_3$ crystals is noted in [27].

In the Mössbauer spectrum (Fig. 6) of a sample heat-treated at 500 °C, and which, according to X-ray diffraction data, is X-ray amorphous (Fig. 2), only a paramagnetic component is observed, which can be represented as two doublets – D1, D2 with isomer shifts (IS), characterizing iron in the +3 oxidation state. The results of processing the Mössbauer spectra of the samples are given in Table 1. A comparison of the quadrupole splitting (QS) values of the doublets QS (D1) = 0.67 and QS (D2) = 1.13 shows that the state of Fe^{3+} ions in the "HT 500 °C" sample, corresponding to doublet D2, has a less symmetrical environment than that corresponding to doublet D1. The hyperfine splitting parameters of these doublets are close to the IS and QS values found for $BiFeO_3$ particles with sizes of 10 – 20 nm [49, 50].

In the Mössbauer spectrum of a sample heat-treated at 515 °C, along with a doublet, the share of which is about 3 %, two superimposed sextets are detected, characteristic of $BiFeO_3$ with magnetic ordering [51, 52]. It should be noted that the disappearance of the D2 doublet, which corresponds to the most asymmetric environment of iron, indicates that the formation of crystalline bismuth orthoferrite occurs due to the crystallization of an amorphous substance in which iron ions are in the most asymmetric environment. The doublet, apparently, can be correlated with the amorphous state of the substance or with crystalline clusters of bismuth orthoferrite so small that they appear as X-ray amorphous.

HT 500 ºC

HT 515 ºC

50 nm

50 nm

10 nm

(a)   (b)

HT 530 °C

50 nm

50 nm

(c)
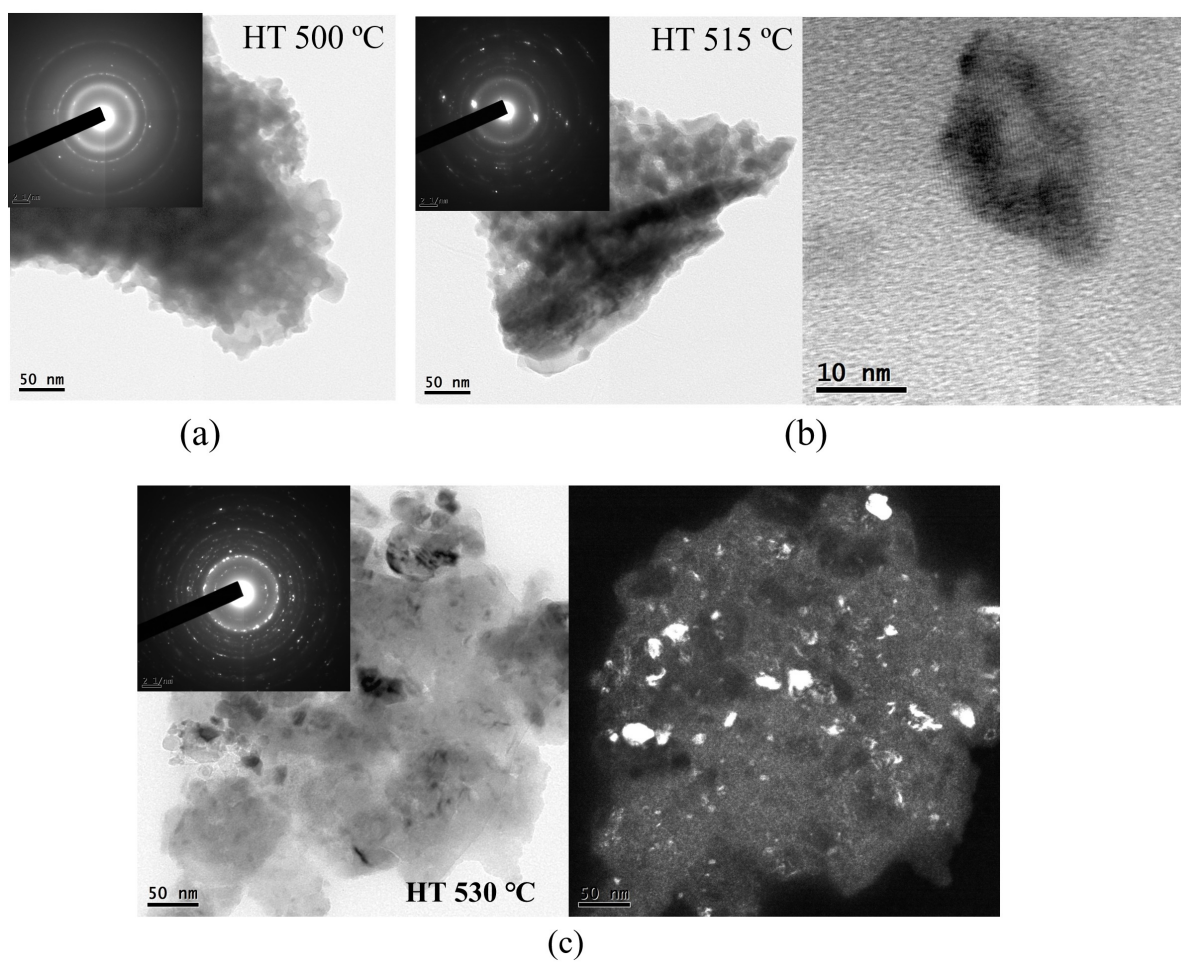
FIG. 4. TEM data of samples heat-treated at 500 (a), 515 (b) and 530 °C (c)

10 nm
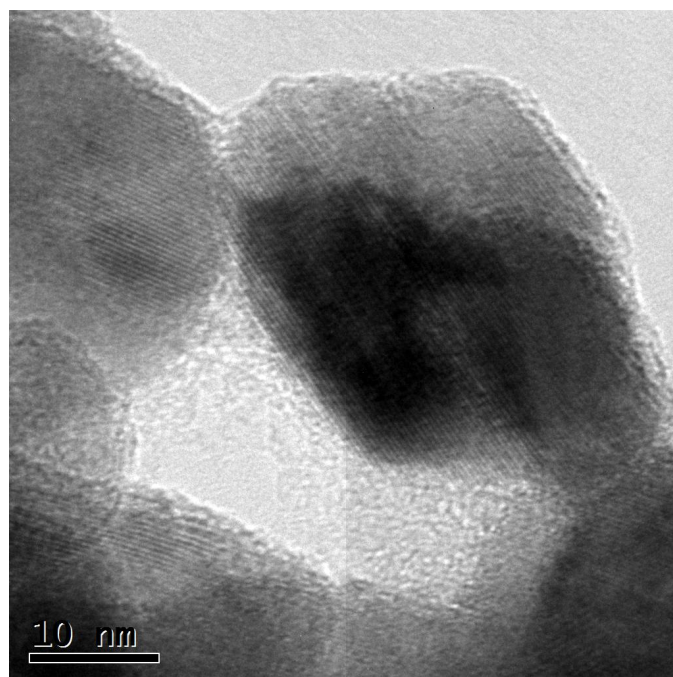
FIG. 5. BiFeO₃ nanocrystals in a sample heat-treated at 530 °C
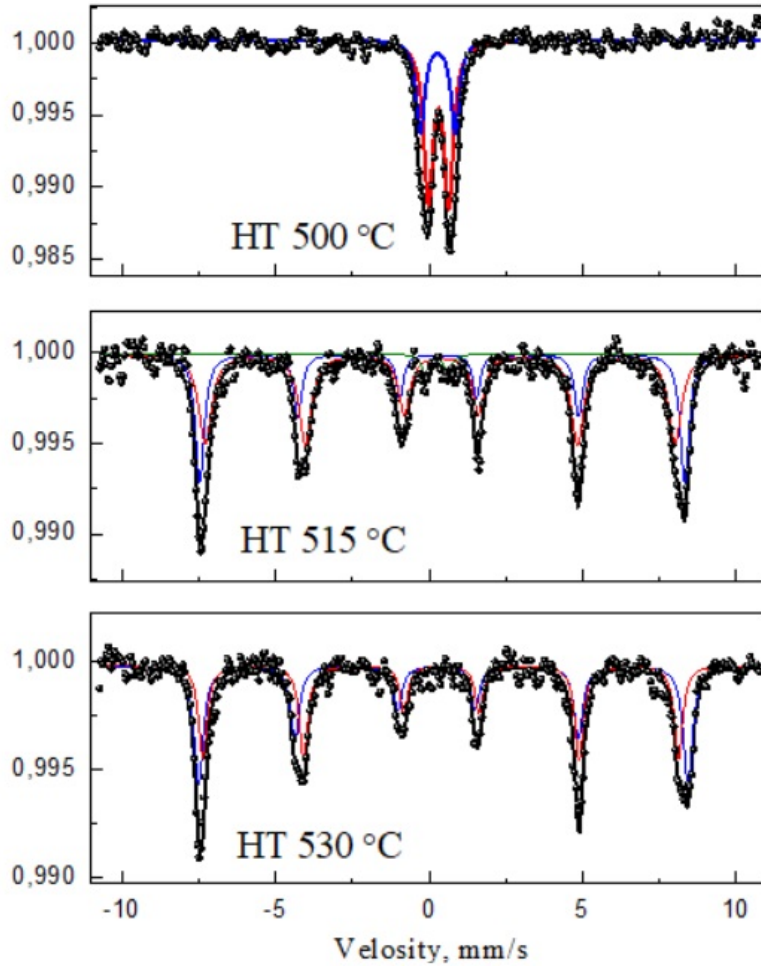
FIG. 6. Mössbauer spectra of samples heat-treated at 500, 515 and 530 °C

In the Mössbauer spectrum of a sample heat-treated at 530 °C, two sextets are observed; there is no doublet component.

TABLE 1. Parameters of Mössbauer spectra of samples at room temperature

Sample	Component	Isomer shift, IS [mm/s]	Quadrupole splitting, QS [mm/s]	Effective magnetic field H_{eff} [T]	Integral intensities ratio [%]
HT 500 °C	Doublet 1	0.31 ± 0.01	0.67 ± 0.02	–	65
	Doublet 2	0.28 ± 0.01	1.13 ± 0.03	–	35
HT 515 °C	Doublet 1	0.24 ± 0.04	0.74 ± 0.08	–	3
	Sextet 1	0.36 ± 0.01	-0.13 ± 0.02	49.1 ± 0.07	39
	Sextet 2	0.38 ± 0.01	0.04 ± 0.02	47.6 ± 0.13	58
HT 530 °C	Sextet 1	0.35 ± 0.01	-0.21 ± 0.01	49.5 ± 0.05	52
	Sextet 2	0.39 ± 0.01	0.02 ± 0.01	48.1 ± 0.05	48

Figure 7 shows the M–H magnetization curve of bismuth ferrite nanopowders heat-treated at 530 °C.

The obtained data shows that the curve does not reach saturation, which indicates the dependence of the magnetic moment of the particles on the applied magnetic field. The values of saturation magnetization and residual magnetization

are 2.31 and 0.48 emu/g, respectively. This magnetic behavior of the sample is explained by the small size of the crystallites (14±7 nm). It was shown in [53] that the magnetization depends on the size of the crystallites and can reach very high values when the crystallite sizes decrease to nanometer values, which was explained by surface effects [53, 54]. The particle size can also affect the anisotropy and coercive force of bismuth ferrite. Small particles usually exhibit a higher coercive force due to an increase in surface anisotropy [55].
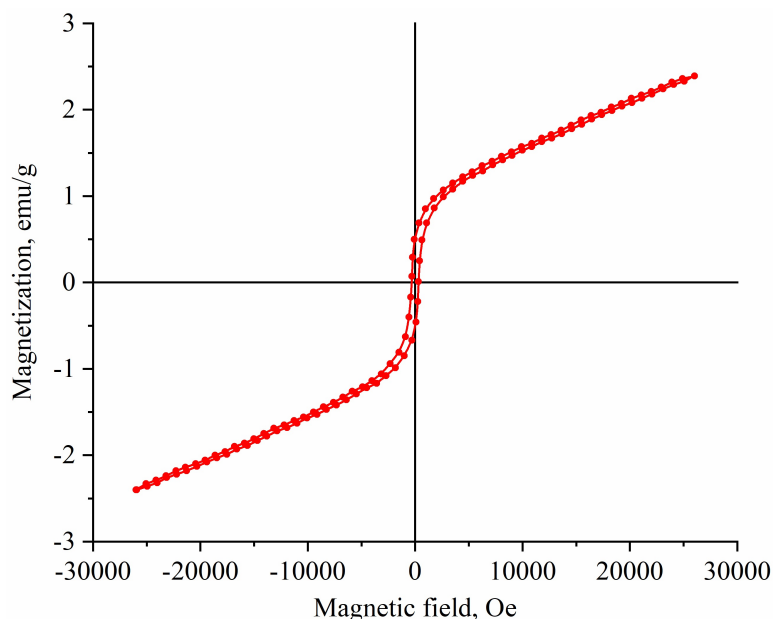
FIG. 7. M-H loop of "HT 530 °C" nanopowder

In the diffuse reflectance spectra (DRS) of the samples (Fig. 8a), absorption bands can be observed in the visible region at 500 nm and 650 nm, which suggests their potential as visible light photocatalysts. The sample calcinated at 530 °C demonstrates the most intensive absorption indicating it as perspective material for visible-light-driven photocatalytic processes.

The absorbance spectra indicated the having direct bang gaps for all samples. The obtained spectra were recalculated to Tauc plot by the Kubelka–Munk function to determine the bang gap values (Fig. 8b). The band gap energy (E_g) for the samples calcinated at 530, 515, and 500 °C were 1.82 eV, 1.86 eV, and 1.91 eV, respectively. The obtained values are close to the previous research data for the sample calcinated at 500 °C ($E_g = 2.16$ eV [48]; $E_g = 2.04$ eV [56]), and lower for other samples.
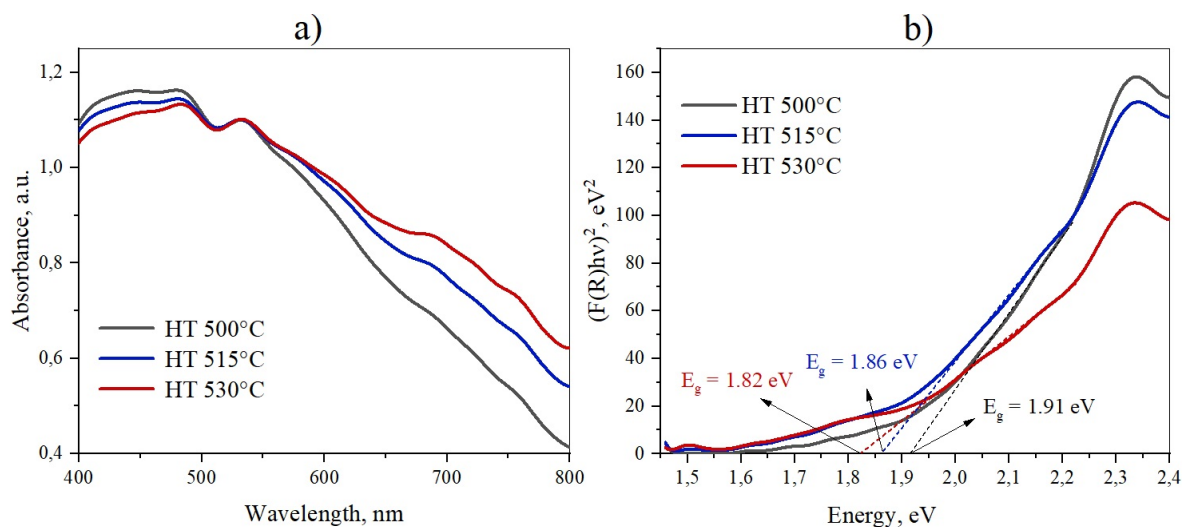
FIG. 8. Diffuse reflectance spectra (a) and Tauc plots (b) of the samples calcinated at different temperatures

A study of the photocatalytic activity of the samples without addition of hydrogen peroxide showed that methyl violet decolorization occurs with an efficiency of 9.8 – 16.1 % (Fig. 9b). The change in color intensity under the action of the

most effective catalyst is shown in Fig. 9a. Linearization of the kinetic curves demonstrated a pseudo-first order reaction for the photocatalytic decolorization of methyl violet (Fig. 9c), and the kinetic constants determined as the slope of the plot were 0.0011, 0.0012, 0.0016 min^{-1} for samples HT 500 °C, HT 515 °C and HT 530 °C, respectively (inset in Fig. 9c). The resulting samples have a relatively low efficiency during the photodegradation of methyl violet, which may be due to the small specific surface area and macroporous structure.
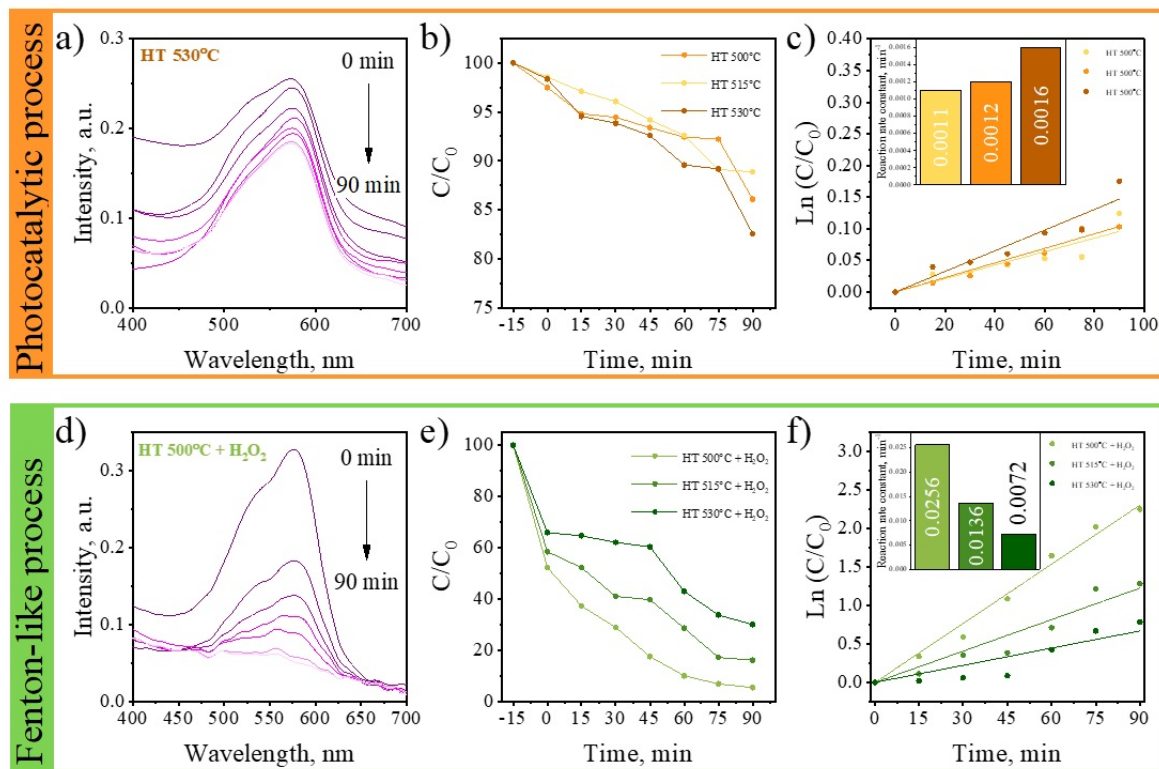
FIG. 9. Photocatalytic activity of samples in classical (a–c) and Fenton-like (d–f) degradation processes of methyl violet: degradation of the dye under the influence of HT 530 °C (a) and HT 500 °C + H_2O_2 (d); kinetic curves (b, e) and linearized kinetic curves (c, f); rate constants for the dye degradation reaction (insets in graphs (c, f))

    The photocatalytic activity of the obtained samples was also studied in the process of Fenton-like degradation of methyl violet. With the addition of hydrogen peroxide, the dye decolorization efficiency increased significantly and was 69.9 % for HT 530 °C + H_2O_2, 83.8 % for HT 515 °C + H_2O_2 and 94.5 % for HT 500 °C + H_2O_2 (Fig. 9e). For the latter, spectra are shown presenting the change in the color intensity of the solution depending on the irradiation time (Fig. 9d), indicating almost complete decomposition of the dye. The pseudo-first order kinetic reaction constants determined from the linearized kinetic curves (Fig. 9f) were 0.0265, 0.0136, 0.0072 min^{-1} for the HT 500 °C + H_2O_2, HT 515 °C + H_2O_2 and HT 530 °C + H_2O_2 samples, respectively. (inset in Fig. 9f). The values of pseudo-first order reaction rate constants obtained for the Fenton-like decomposition of methyl violet are 5 – 20 times higher than similar constants for the photocatalytic process (without the addition of hydrogen peroxide). This increase in photocatalytic efficiency is associated with the high activity of ferrites in general and bismuth ferrite in particular in Fenton-like oxidation processes due to the presence of Fe^{3+} and Bi^{3+} ions [57–59].

    It was also shown that the HT 500 °C + H_2O_2 sample, containing the largest proportion of the amorphous phase, exhibits greater Fenton photocatalytic activity compared to other samples. The increase in activity in this case, as shown in previous studies [60], is explained by the fact that a certain amount of amorphous component in photocatalysts can significantly increase the efficiency of electron-hole pair separation, visible light absorption and adsorption properties.

5.   Conclusion

    To obtain bismuth orthoferrite, hydroxide precipitation was used in the one-step microreactor with intensively swirling flows, followed by heat treatment of co-precipitated bismuth and iron hydroxides.

    It has been shown that when thermally treating hydroxide precipitates for 1 minute at a temperature of 530 °C, $BiFeO_3$ nanocrystals with an average crystallite size of 14±7 nm are formed. It has been revealed that the resulting $BiFeO_3$ nanopowder is represented by agglomerates of individual nanoparticles. The saturation magnetization and remanent magnetization values of these bismuth orthoferrite nanoparticles are 2.31 and 0.48 emu/g, respectively.

The following mechanism of growth of bismuth orthoferrite particles is proposed: after dehydration of a mixture of amorphous bismuth and iron hydroxides and the formation of crystalline BiFeO$_3$ nuclei, their growth occurs due to the coherent attachment of clusters, which make up the amorphous phase, to crystalline particles of bismuth ferrite. Crystal growth stops if the growing BiFeO$_3$ crystals collide with each other without oriented accretion along the edges or due to exhaustion of the amorphous substance inside which the BiFeO$_3$ crystals grow.

According to the DRS results, band gap energy for the samples calculated at 530, 515, and 500 °C were 1.82, 1.86, and 1.91 eV, respectively, which ensures strong absorption of visible light by the samples.

The photocatalytic and Fenton-photocatalytic activity of the obtained nanocrystalline powders was studied during the oxidation of methyl violet. The sample showed higher photocatalytic activity in the X-ray amorphous state compared with nanocrystalline BiFeO$_3$ in the process of Fenton-like discoloration of methyl violet under the action of visible light with reaction rate constants of the pseudo-first order 0.0256 and 0.0072 min^{-1}, respectively.

References

[1] Kharbanda S., Dhanda N., Sun A.-C.A., Thakur A., Thakur P. Multiferroic perovskite bismuth ferrite nanostructures: A review on synthesis and applications. *Journal of Magnetism and Magnetic Materials*, 2023, **572**, P. 170569.

[2] Krishnamoorthy A., Hannah I., Maruthasalamoorthy S., Nirmala R., Punithavelan N., Navamathavan R. Review – State of the Art of the Multi-functional Bismuth Ferrite: Synthesis Method and Applications. *ECS Journal of Solid State Science and Technology*, 2022, **11**, P. 043010.

[3] Ghuge R.S., Shinde M.D., Rane S.B. Bismuth-Based Gas Sensors: A Comprehensive Review. *Journal of Electronic Materials*, 2021, **50**(11), P. 6060–6072.

[4] Gervits N.E., Tkachev A.V., Zhurenko S.V., Gunbin A.V., Bogach A.V., Lomanova N.A., Danilovich D.P., Pavlov I.S., Vasiliev A.L., Gippius A.A. The size effect of BiFeO$_3$ nanocrystals on the spatial spin modulated structure. *Physical Chemistry Chemical Physics*, 2023, **25**(37), P. 25526–25536.

[5] Kravtsova P.D., Tomkovich M.V., Volkov M.P., Buryanenko I.V., Semenov V.G., Popkov V.I., Lomanova N.A. Magnetic properties of nanocrystalline materials based on the system (1-x)BiFeO$_3$-(x)YFeO$_3$. *Physics of the Solid State*, 2023, **65**(12), P. 2120–2123.

[6] Chinchay-Espino H.A., Montes-Albino G.M., Morales-Cruz C.M., Dobbertin-Sanchez S.E., Rojas-Flores S. Effect of Cobalt Substitution on the Structural and Magnetic Properties of Bismuth Ferrite Powders. *Crystals*, 2022, **12**, P. 1058.

[7] Zhao X., Menzel S., Polian I., Schmidt H., Du N. Review on Resistive Switching Devices Based on Multiferroic BiFeO$_3$. *Nanomaterials*, 2023, **13**, P. 1325.

[8] Dang T.T., Schell J., Boa A.G., Lewin D., Marschick G., Dubey A., Escobar-Castillo M., Noll C., Beck R., Zyabkin D.V., Glukhov K., Yap I.C.J., Mokhles G. A., Lupascu D.C. Temperature dependence of the local electromagnetic field at the Fe site in multiferroic bismuth ferrite. *Physical Review B*, 2022, **106**(5), P. 054416.

[9] Taha G.M., Rashed M.N., El-Sadek M.S.A., Moghazy M.A.E. Multiferroic BiFeO$_3$ dithizone functionalized as optical sensor for detection and determination of some heavy metals in environmental samples. *Bulletin of Materials Science*, 2021, **44**(2), P. 122.

[10] Ahmed I., Naz I., Morley N., Shabbir S., Maraj M., Ismail A.G., Anwar H., Ahmad F. Experimental and DFT investigation of structural and optical properties of lanthanum substituted bismuth ferrites. *Physica B: Condensed Matter.*, 2023, **661**, P. 414927.

[11] Nguyen K., Nguyen. C., Pham C., Lim D., Nguyen Q.-B., Le H., Mai N., Dao N. Kinetics and mechanism of photocatalytic degradation of rhodamine B on nanorod bismuth ferrite perovskite prepared by hydrothermal method. *Research on Chemical Intermediates*, 2022, **49**, P. 57–72.

[12] Cadenbach T., Sanchez V., Chiquito Ríos D., Debut A., Vizuete K., Benitez M.J. Hydrothermal Synthesis of Bismuth Ferrite Hollow Spheres with Enhanced Visible-Light Photocatalytic Activity. *Molecules*, 2023, **28**, P. 5079.

[13] Zhou T., Zhai T., Shen H., Wang J., Min R., Ma K., Zhang G. Strategies for enhancing performance of perovskite bismuth ferrite photocatalysts (BiFeO$_3$): A comprehensive review. *Chemosphere*, 2023, **339**, P. 139678.

[14] Mittal S., Garg S., Bhandari H., Sharma V. A review on recent progressions of Bismuth ferrite modified morphologies as an effective photocatalyst to curb water and air pollution. I*norganic Chemistry Communications*, 2022, **144**, P. 109834.

[15] Ceballos-Sanchez O., Sanchez-Martinez A., Flores- Ruiz F.J., Huerta-Flores A.M., Torres-Martínez L.M., Ruelas R, García-Guaderrama M. Study of BiFeO$_3$ thin film obtained by a simple chemical method forthe heterojunction-type solar cell design. *Journal of Alloys and Compounds*, 2020, **832**, P. 154923.

[16] Eshore A.N., Dey S., Goswami D.K., Guha P.K. Crystallographic Nanojunctions of Bismuth Ferrite for Unconventional Detection of Carbon Monoxide. *ACS Applied Nano Materials*, 2023, **6**(11), P. 9397–9403.

[17] Dmonte D.J., Bhardwaj A., Wilhelm M., Fischer T., Kuřitka I., Mathur S. Sub PPM Detection of NO$_2$ Using Strontium Doped Bismuth Ferrite Nanostructures. *Micromachines*, 2023, **14**, P. 644.

[18] Ji H., Zhang L., Zhang R. Gas sensitive performance and mechanism of multiferroic BiFeO$_3$ under thermal-magnetic synergetic excitation. *Inorganic Chemistry Communications*, 2023, **150**, P. 110491.

[19] Zhang Y., Zhang H., Zhang J., Guo J., Zhang D. Fast Response and Low Detection Limit of Ammonia Sensor Based on WO$_3$ Nanoparticles-Decorated BiFeO$_3$ Nanoplates. *IEEE Sensors Journal*, 2022, **22**(15), P. 14736–14742.

[20] Egorysheva A.V., Kraev A.S., Gajtko O.M., Baranchikov A.E., Agafonov A.V., Ivanov V.K. Electrorheological Fluids Based on Bismuth Ferrites BiFeO$_3$ and Bi$_2$Fe$_4$O$_9$. *Russian Journal of Inorganic Chemistry,* 2020, **65**(8), P. 1253–1263.

[21] Li Y., Zhang X., Chen L., Sun H., Zhang H., Si W., Wang W., Wang L., Li J. Enhanced magnetic and photocatalytic properties of BiFeO$_3$ nanotubes with ultrathin wall thickness. *Vacuum*, 2021, **184**, P. 109867.

[22] Egorysheva A.V., Milenov T.I., Ellert O.G., Avdeev G.V., Rafailov P.M., Efimov N.N., Novotortsev V.M. Magnetic glasseceramics containing multiferroic BiFeO$_3$ crystals. *Solid State Science*, 2015, **40**, P. 31–35.

[23] Gao X., Wang Y., Wang Q., Wu X., Zhang W., Zong M., Zhang L. Facile synthesis of a novel flower-like BiFeO$_3$ microspheres/graphene with superior electromagnetic wave absorption performances. *Ceramics International*, 2019, **45**(3), P. 3325–3332.

[24] Yastrebov S.G., Lomanova N.A. Specific Features in the Interaction between BiFeO$_3$ Nanoclusters Synthesized by Solution Combustion. *Technical Physics Letters*, 2021, **47**(1), P. 1–4.

[25] Alikhanov N.M.-R., Rabadanov M.Kh., Orudzhev F.F., Gadzhimagomedov S.Kh., Emirov R.M., Sadykov S.A., Kallaev S.N., Ramazanov S.M., Abdulvakhidov K.G., Sobola D. Size-dependent structural parameters, optical, and magnetic properties of facile synthesized pure-phase BiFeO$_3$. *Journal of Materials Science: Materials in Electronics*, 2021, **32**, P. 13323–13335.

[26] Mhamad S.A., Ali A.A., Mohtar S.S., Aziz F., Aziz M., Jaafar J., Yusof N., Salleh W.N.W., Ismail A.F., Chandren S. Synthesis of bismuth ferrite by sol-gel auto combustion method: Impact of citric acid concentration on its physicochemical properties. *Materials Chemistry and Physics*, 2022, **282**, P. 125983.

[27] Proskurina O.V., Tomkovich M.V., Bachina A.K., Sokolov V.V., Danilovich D.P., Panchuk V.V., Semenov V.G., Gusarov V.V. Formation of Nanocrystalline $BiFeO_3$ under Hydrothermal Conditions. *Russian Journal of General Chemistry*, 2017, **87**(11), P. 2507–2515.

[28] Rouhani Z., Karimi-Sabet J., Mehdipourghazi M., Hadi A., Dastbaz A. Response surface optimization of hydrothermal synthesis of Bismuth ferrite nanoparticles under supercritical water conditions: Application for photocatalytic degradation of Tetracycline. *Environmental Nanotechnology, Monitoring & Management*, 2019, **11**, P. 100198.

[29] Wang Z.-B., Aldalbahi A., Ahamad T., Alshehri S.M., Feng P.X. Preparation of $BiFeO_3$ and its photoelectric performance as photoanode of DSSC. *Ceramics International*, 2021, **47**(19), P. 27565–27570.

[30] Xiaoyan Sun, Zhongwu Liu, Hongya Yu, Zhigang Zheng, Dechang Zeng, Facile synthesis of $BiFeO_3$ nanoparticles by modified microwave-assisted hydrothermal method as visible light driven photocatalysts. *Materials Letters*, 2018, **219**, P. 225–228.

[31] Tuluk A., Brouwer H., van der Zwaag S. Controlling the Oxygen Defects Concentration in a Pure $BiFeO_3$ Bulk Ceramic. *Materials*, 2022, **15**, P. 6509.

[32] Gil-González E., Perejón A., Sánchez-Jiménez P.E., Sayagués M.J., Raj R., Pérez-Maqueda L.A. Phase-pure $BiFeO_3$ produced by reaction flash-sintering of Bi_2O_3 and Fe_2O_3. *Journal of Materials Chemistry A*, 2018, **6**(13), P. 5356–5366.

[33] Carranza-Celis D., Cardona-Rodríguez A., Narváez J., Moscoso-Londono O., Muraca D., Knobel M., Ornelas-Soto N., Reiber A., Ramírez J.G. Control of Multiferroic properties in $BiFeO_3$ nanoparticles. *Scientific Reports*, 2019, **9**, P. 3182.

[34] Pedro-García F., Sánchez-De Jesús F., Cortés-Escobedo C.A., Barba-Pingarrón A., Bolarín-Miró A.M. Mechanically assisted synthesis of multi-ferroic $BiFeO_3$: Effect of synthesis parameters. *Journal of Alloys and Compounds*, 2017, **711**(2004), P. 77–84.

[35] Selbach S.M., Einarsrud M.-A., Grande T. On the Thermodynamic Stability of $BiFeO_3$. *Chemistry of Materials*, 2009, **21**(1), P. 169–173.

[36] Denisov V.M., Belousova N.V., Zhereb V.P., Denisova L.T., Skorikov V.M. Oxide Compounds of $Bi_2O_3 - Fe_2O_3$ System I. The Obtaining and Phase Equilibriums. *Journal of Siberian Federal University. Chemistry*, 2012, **5**(2), P. 146–167.

[37] Pikula T., Szumiata T., Siedliska K., Mitsiuk V.I., Panek R., Kowalczyk M., Jartych E. The Influence of Annealing Temperature on the Structure and Magnetic Properties of Nanocrystalline $BiFeO_3$ Prepared by Sol–Gel Method. *Metallurgical and Materials Transactions A*, 2022, **53**, P. 470–483.

[38] Stankiewicz A.I., Moulijn J.A. Process intensification: Transforming chemical engineering. *Chemical Engineering Progress*, 2000, **96**(1), P. 22–34.

[39] Abiev R.S. Impinging-Jets Micromixers and Microreactors: State of the Art and Prospects for Use in the Chemical Technology of Nanomaterials (Review). *Theoretical Foundations of Chemical Engineering*, 2020, **54**(6), P. 1131–1147.

[40] Proskurina O.V., Sivtsov E.V., Enikeeva M.O., Sirotkin A.A., Abiev R.Sh., Gusarov V.V. Formation of rhabdophane-structured lanthanum orthophosphate nanoparticles in an impinging-jets microreactor and rheological properties of sols based on them. *Nanosystems: Physics, Chemistry, Mathematics*, 2019, **10**(2), P. 206–214.

[41] Bałdyga J., Jasińska M., Orciuch W. Barium Sulphate Agglomeration in a Pipe – An Experimental Study and CFD Modeling. *Chemical Engineering & Technology*, 2003, **26**(3), P. 334–340.

[42] Almjasheva O.V., Popkov V.I., Proskurina O.V., Gusarov V.V. Phase formation under conditions of self-organization of particle growth restrictions in the reaction system. *Nanosystems: Physics, Chemistry, Mathematics*, 2022, **13**(2), P. 164–180.

[43] Proskurina O.V., Abiev R.S., Danilovich D.P., Panchuk V.V., Semenov V.G., Nevedomsky V.N., Gusarov V.V. Formation of nanocrystalline $BiFeO_3$ during heat treatment of hydroxides co-precipitated in an impinging-jets microreactor. *Chemical Engineering and Processing – Process Intensification*, 2019, **143**, P. 107598.

[44] Lomakin M.S., Proskurina O.V., Abiev R.Sh., Leonov A.A., Nevedomskiy V.N., Voznesenskiy S.S., Gusarov V.V. Pyrochlore phase in the $Bi_2O_3–Fe_2O_3–WO_3–(H_2O)$ system: physicochemical and hydrodynamic aspects of its production using a microreactor with intensively swirled flows. *Advanced Powder Technology*, 2023, **34**, P. 104053.

[45] Abiev R.Sh., Makusheva I.V. Effect of Macro- and Micromixing on Processes Involved in Solution Synthesis of Oxide Particles in High-Swirl Microreactors. *Theoretical Foundations of Chemical Engineering*, 2022, **56**(2), P. 141–151.

[46] Proskurina O.V., Sokolova A.N., Sirotkin A.A., Abiev R.Sh., Gusarov V.V. Role of Hydroxide Precipitation Conditions in the Formation of Nanocrystalline $BiFeO_3$. *Russian Journal of Inorganic Chemistry*, 2021, **66**(2), P. 163–169.

[47] Proskurina O.V., Abiev R.Sh., Nevedomskiy V.N. Influence of using different types of microreactors on the formation of nanocrystalline $BiFeO_3$. *Nanosystems: Physics, Chemistry, Mathematics*, 2023, **14**(1), P. 120–126.

[48] Li X., Tang Z., Ma H., Wu F., Jian R. PVP-assisted hydrothermal synthesis and photocatalytic activity of single-crystalline $BiFeO_3$ nanorods. *Applied Physics A*, 2019, **125**, P. 598.

[49] Ortiz-Quiñonez J.L., Díaz D., Zumeta-Dubé I., Arriola-Santamaría H., Betancourt I., Santiago-Jacinto P., Nava-Etzana N. Easy Synthesis of High-Purity $BiFeO_3$ Nanoparticles: New Insights Derived from the Structural, Optical, and Magnetic Characterization. *Inorganic Chemistry*, 2013, **52**(18), P. 10306–10317.

[50] Park T.-J., Papaefthymiou G.C., Viescas A.J., Moodenbaugh A.R., Wong S.S. Size-Dependent Magnetic Properties of Single-Crystalline Multiferroic $BiFeO_3$. *Nanoparticles*, 2007, **7**(3), P. 766–772.

[51] Lomanova N.A., Tomkovich M.V., Sokolov V.V., Ugolkov V.L., Panchuk V.V., Semenov V.G., Pleshakov I.V., Volkov M.P., Gusarov V.V. Thermal and magnetic behavior of $BiFeO_3$ nanoparticles prepared by glycine-nitrate combustion. *Journal of Nanoparticle Research*, 2018, **20**, P. 17.

[52] Freitas V.F., Grande H.L.C., de Medeiros S.N., Santos I.A., Cótica L.F., Coelho A.A. Structural, microstructural and magnetic investigations in high-energy ball milled $BiFeO_3$ and $Bi_{0.95}Eu_{0.05}FeO_3$ powders. *Journal of Alloys and Compounds*, 2008, **461**(1-2), P. 48–52.

[53] Lomanova N.A., Panchuk V.V., Semenov V.G., Pleshakov I.V., Volkov M.P., Gusarov V.V. Bismuth orthoferrite nanocrystals: magnetic characteristics and size effects. *Ferroelectrics*, 2020, **569**(1), P. 240–250.

[54] Juwita E., Sulistiani F.A., Darmawan M.Y., Istiqomah N.I., Suharyadi E. Microstructural, optical, and magnetic properties and specific absorption rate of bismuth ferrite/SiO_2 nanoparticles. *Materials Research Express*, 2022, **9**, P. 076101.

[55] Ramazanov S., Sobola D., Orudzhev F., Knapek A., Polcak J., Potocek M., Kaspar P., Dallaev R. Surface Modification and Enhancement of Ferromagnetism in $BiFeO_3$ Nanofilms Deposited on HOPG. *Nanomaterials*, 2020, **10**(10), P. 1990.

[56] Thamizharasan G., Eithiraj R.D., Enhtuwshin E., Kim S.J., Sahu N.K., Nayak A.K., Han H.S. Computational and Experimental Study on Electronic Band Structure of Bismuth Ferrite: A Promising Visible Light Photocatalyst. *Ceramist*, 2020, **23**(4), P. 350–357.

[57] Wang N., Zheng T., Zhang G., Wang P. A review on Fenton-like processes for organic wastewater treatment. *Journal of Environmental Chemical Engineering*, 2016, **4**(1), P. 762–787.

[58] Mao J., Quan X., Wang J., Gao C., Chen S., Yu H., Zhang Y. Enhanced heterogeneous Fenton-like activity by Cu-doped $BiFeO_3$ perovskite for degradation of organic pollutants. *Frontiers of Environmental Science & Engineering*, 2018, **12**(6), P. 10.

[59] Dhanalakshmi R., Muneeswaran M., Vanga P.R.; Ashok M.; Giridharan N.V. Enhanced photocatalytic activity of hydrothermally grown BiFeO₃ nanostructures and role of catalyst recyclability in photocatalysis based on magnetic framework. *Applied Physics A*, 2016, **122**(1), P. 13.

[60] Liang C., Liu Y., Li K., Wen J., Xing S., Ma Z., Wu Y. Heterogeneous photo-Fenton degradation of organic pollutants with amorphous Fe-Zn-oxide/hydrochar under visible light irradiation. *Separation and Purification Technology*, 2017, **188**, P. 105–111.

Information about the authors:

Olga V. Proskurina – Ioffe Institute, 194021 St. Petersburg, Russia; St. Petersburg State Institute of Technology, 190013 St. Petersburg, Russia; ORCID 0000-0002-2807-375X; proskurinaov@mail.ru

Ksenia I. Babich – Ioffe Institute, 194021 St. Petersburg, Russia; St. Petersburg State Institute of Technology, 190013 St. Petersburg, Russia; ORCID 0009-0000-2239-7721; babich3111@gmail.com

Sofia M. Tikhanova – Ioffe Institute, 194021 St. Petersburg, Russia; St. Petersburg State Institute of Technology, 190013 St. Petersburg, Russia; ORCID 0000-0002-9239-5470; tihanova.sof@gmail.com

Kirill D. Martinson – Ioffe Institute, 194021 St. Petersburg, Russia; St. Petersburg State Institute of Technology, 190013 St. Petersburg, Russia; ORCID 0000-0001-9313-4267; martinsonkirill@mail.ru

Vladimir N. Nevedomskiy – Ioffe Institute, 194021 St. Petersburg, Russia; ORCID 0000- 0002-7661-9155; nevedom@mail.ioffe.ru

Valentin G. Semenov – St. Petersburg State University, 26, Universitetsky Ave., Petergof, 198504 St. Petersburg, Russia; ORCID 0000-0002-1530-7289; val_sem@mail.ru

Rufat Sh. Abiev – Ioffe Institute, 194021 St. Petersburg, Russia; St. Petersburg State Institute of Technology, 190013 St. Petersburg, Russia; ORCID 0000-0003-3571-5770; abiev.rufat@gmail.com

Victor V. Gusarov – Ioffe Institute, 194021 St. Petersburg, Russia; ORCID 0000-0003-4375-6388; victor.v.gusarov@gmail.com

Conflict of interest: the authors declare no conflict of interest.